Supplementary Information for A Non-destructive UV Raman Characterisation Platform to Enable Insight into the Mechanism of Reversible Ultraviolet-Induced Degradation (UVID) in TOPCon Solar Cells

SI 1. Summary of I-V performance of tested TOPCon cells.

The parameters of I-V performance obtained from the tested reference, UVID and LSIR cells are summarized in Table 1.

Table 1. summary of typical parameters of tested TOPCon solar cells

Parameters	Values			Change ratio to reference	
	Reference	UVID	LSIR	after UVID	after LSIR
PCE (%)	24.03	22.14	23.86	-7.87%	-0.69%
V_{OC} (mV)	734	689	724	-6.06%	-1.38%
I_{SC} (A)	13.51	13.32	13.49	-1.40%	-0.13%
FF (%)	80.30	79.87	80.97	-0.53%	0.84%

SI 2. IQE of reference, UVID and LSIR cells

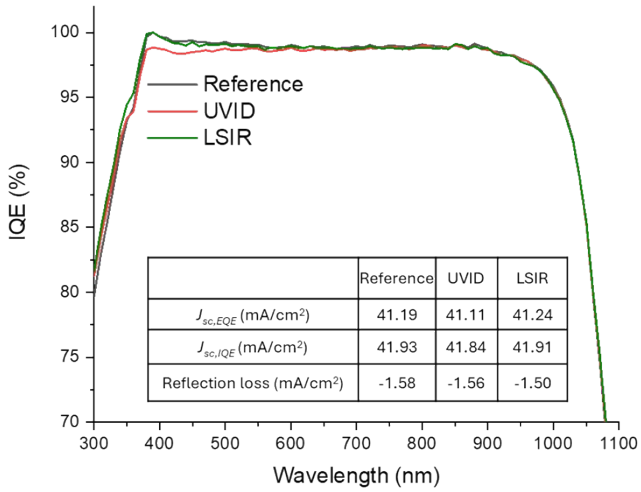

Fig. S1. IQE spectra of reference, UVID and LSIR cell respectively. The table inserted summarises the calculated current values (mA/cm^2) based on the spectra of QEQ, IQE and Reflection (R).

SI 3. UV Raman spectra

Typical Raman curves of tested cells are shown in Fig. S2 a&b. To obtain high-quality Raman curves and verify the validity of this UV Raman method, some details and explanations regarding UV Raman measurement are given. First, local heating is worth noting in Raman test. However, the 325 nm UV laser used in this research is much weaker in intensity than the visible laser, such as 514nm. The tested area before and after in-situ Raman test does not show any change in appearance as shown in Fig. S2 c&d. In addition, Si has a thermal conductivity of 140 –150 W/(m·K), and the laser exposure area is only ~ 22 um in diameter on the surface of a large piece of TOPCon cell (> 5×5 cm^2). Therefore, the heat can quickly dissipate rather than accumulate during the UV Raman test. In addition, the Raman mapping (Fig. S2 e&f) showed exactly the laser exposure area where Si-B bonds are changed by UV exposure. With the UV exposure, the obtained Raman peak will become narrower and thus lead to smaller under-peak area, which explains that the UV laser exposure area appears darker in the mapping. Control in-situ Raman experiments were also performed on intrinsic Si wafer, the Si peak does not demonstrate any change in position and width, further confirming the observed change in UVID cells is caused by the change in the states of Boron dopants.

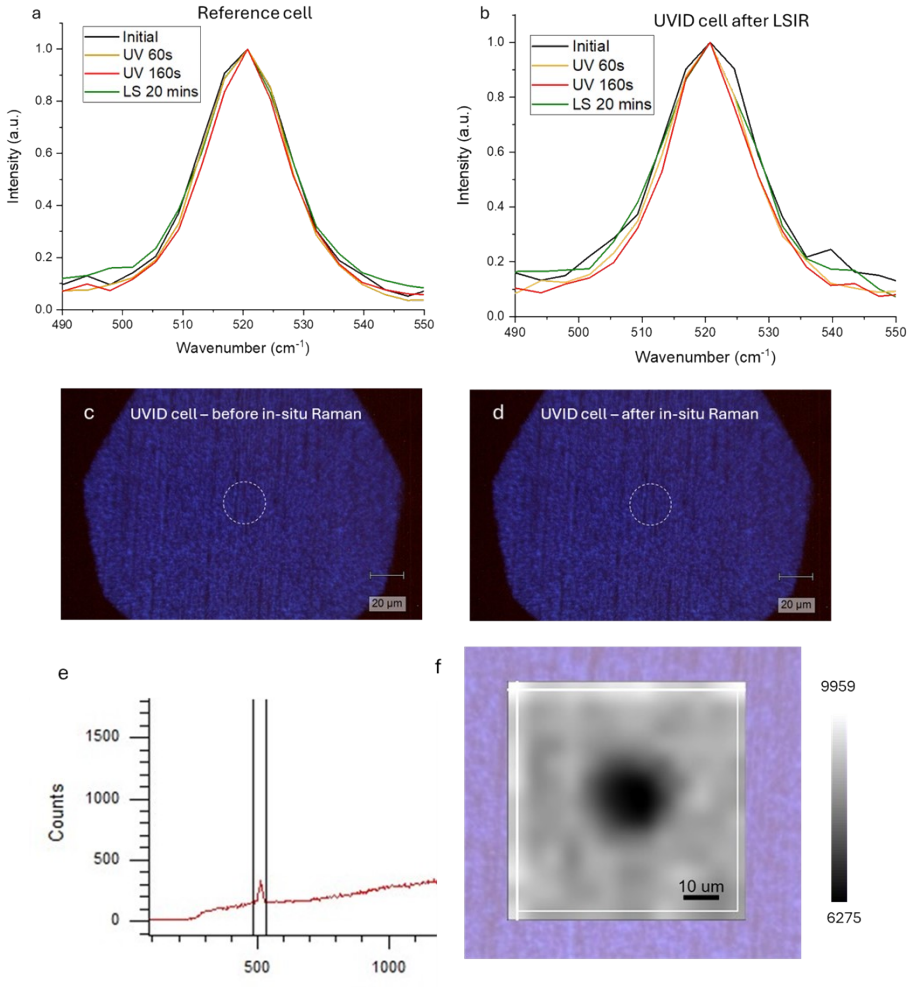

Fig. S2. In-situ UV Raman spectra of a, reference cell and b, UVID and LSIR cell under different treatments during in-situ UV Raman monitoring. c & d are optical images of a UVID cell taken at the same UV laser-exposed area before and after in-situ UV Raman test. e, a typical Raman curve correlating to a pixel in Raman mapping. f, Raman mapping of the UV laser exposure spot obtained by calculating of the area under Si Peak as marked in e.

SI 4. Atom probe tomography analysis of Reference and UVID cells

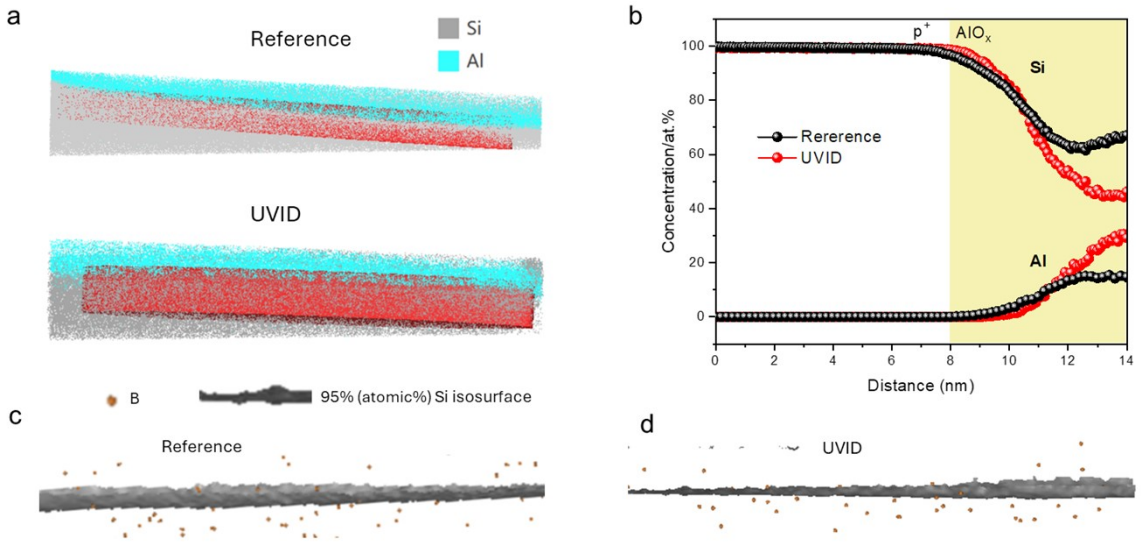

Fig. S3. a, APT 3D reconstruction maps of Reference and UVID cells, showing the spatial distribution of silicon (grey) and aluminum (blue) and red cylinders indicate the chosen region of interest for 1D concentration profile analysis. b, 1D concentration profiles from red cylinders highlighted in a. c & d are 3D reconstructions of B distribution of reference and UVID cells near the AlO_x/Si interface which can be identified using a 95% Si isosurface.

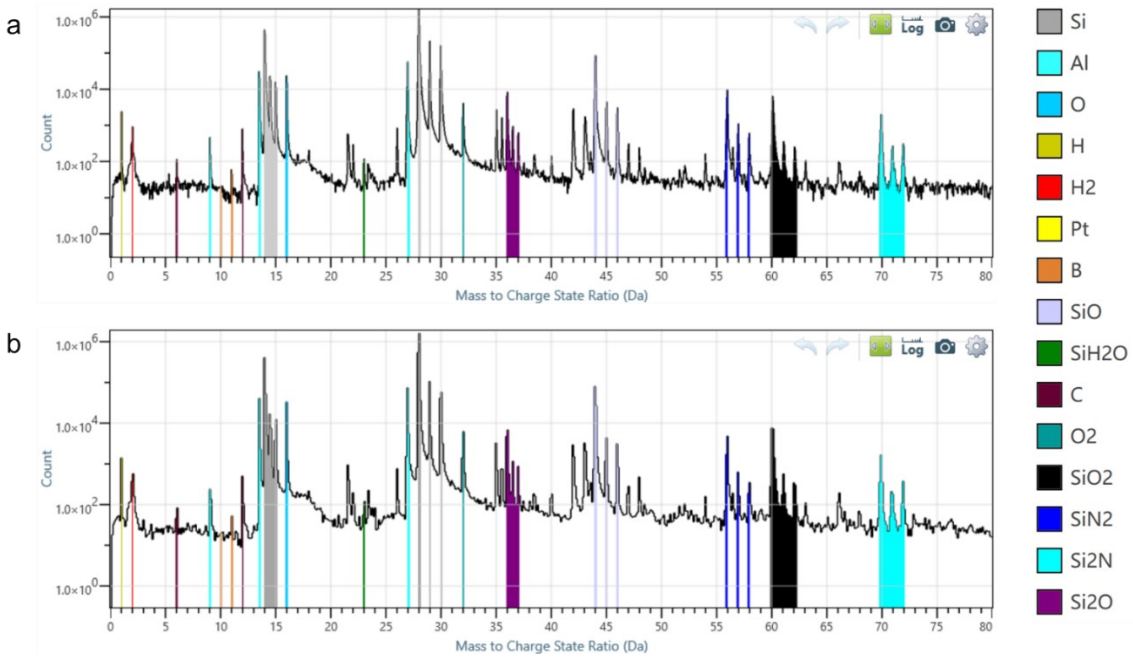

Fig. S4. Mass spectrum for the APT dataset. a, Reference cell. b, UVID cell.

To elucidate the element distribution along the top surface layer of reference and UVID cells, atom probe tomography (APT) is a versatile tool which provides high spatial resolution and sensitivity of all elements including light elements such as hydrogen and boron. First, 3D reconstruction maps were acquired for both cells as shown in Fig. S4a. Then the AlO_x and p^+ interface was identified by creating an isoconcentration surface of Al (8 at.%) and inserting a 14 nm long red cylinder (z axis perpendicular to the isoconcentration surface). 1D concentration profiles in Fig.S4b indicates an increased Al and a declined Si concentration starts from 8nm for both cells, which indicates an interface of $AlO_{x,}$ and p^+ was established at 8 nm position and left part is p^+ while right part is $AlO_{x.}$

The mass spectra for both cells are shown in Fig. S5. Both spectra demonstrate significant counts of H^+ (1 Da) and H_2^+(2 Da) compared to background signal level, confirming the reliability of H existence in the matrix of cells. B^+ (10 Da and 11 Da) strictly follow the isotope abundances of boron as well.

It is also worth mentioning that the apparent differences in hydrogen concentration between the reference and UVID samples observed at distances of approximately 12.5–14 nm can be attributed to local magnification effects during the APT analysis and subsequent 3D reconstruction. These effects arise from the different evaporation fields of AlO_x and Si at the interface: the higher evaporation field of AlO_x compared with Si leads to an apparent elongation of the AlO_x layer along the tip axis in the reconstructed volume. Furthermore, the magnitude of this effect can vary between APT tips, as it is challenging to reproduce identical tip geometries for specimens prepared on textured Si surfaces with pyramidal morphology. As a consequence, the reconstructed hydrogen concentration and its apparent spatial distribution within the AlO_x layer may vary.

SI 5. Simulated Impact of Boron Doping Level and Surface Recombination Velocity on Cell Performance

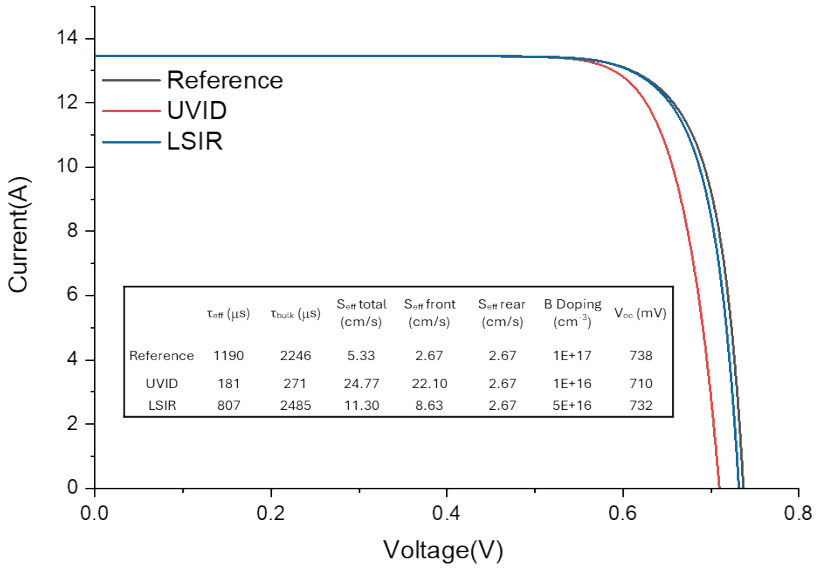

	τ_{eff} (μs)	τ_{bulk} (μs)	S_{eff} total (cm/s)	S_{eff} front (cm/s)	S_{eff} rear (cm/s)	B Doping (cm^{-3})	V_{oc} (mV)
Reference	1190	2246	5.33	2.67	2.67	1E+17	738
UVID	181	271	24.77	22.10	2.67	1E+16	710
LSIR	807	2485	11.30	8.63	2.67	5E+16	732

Fig. S5. The PC1D simulated I–V characteristics of TOPCon cells during UVID and LSIR, used and obtained parameters are inserted as a table.

In the simulations, the effective carrier lifetime (τ_eff) and the bulk lifetime (τ_bulk) were obtained from experimental measurements of the same samples tested in Fig. 1b. The B doping levels were estimated based on our Raman results. The simulation was designed to evaluate the influence of both the surface recombination velocity (SRV) and the boron doping concentration in the p^+ emitter on the V_{OC}. The results indicate that both increased SRV and reduced boron doping contribute to the reduced V_{OC}. More importantly, both the increased SRV and reduced B doping density are caused by the same UVID-induced process, i.e. the migration of H. In this process, breakage of Si-H bond at the AlO_x/Si interface leaves Si dangling bonds, decays the surface passivation and accelerates surface recombination, while formation of Si-H-B deactivates B doping in p^+ emitter under the interface and leads to lower B doping density. After LSIR, the calculated B doping level was effectively recovered, which may lead to an increased FF, which is observed in both experimental and simulated PC1D results.

SI 6. Calculated reflection spectrum of Si cell with reduced Si/N ratio.

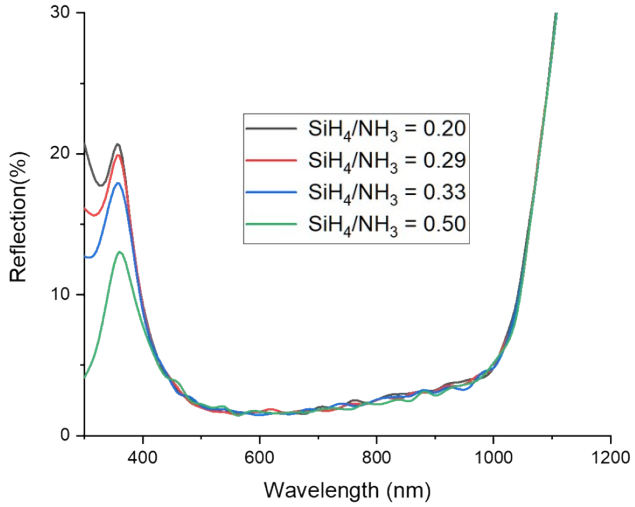

Fig. S6. Ray tracing simulations revealing the impact of SiH_4/NH_3 ratio of SiN_x layer on the optical properties of the TOPCon cells.

The reflection spectra shown in Fig. S3. a represent simulated results for SiN_x layers deposited using various SiH_4/NH_3 gas ratios. The corresponding refractive index of SiN_x for each ratio were taken from a previous study.[1] According to the experimental results in the reference, reducing the gas ratio of SiH_4 during the growth of SiN_x leads to a lower refractive index, which in turn affects the reflectance of the TOPCon cells. In our simulations, we started with a SiH_4/NH_3 ratio of 0.5, which produced results closely matching our initial experimental measurements. We then selected three gas ratios with reduced SiH_4 content. The simulation results clearly show that reducing the SiH_4/NH_3 ratio leads to higher reflection in the short-wavelength region (below 400 nm). This trend indicates that lowering the Si content in the SiNx layer enhances UV light reflection, which may be beneficial for designing solar cells with improved UVID resistance.

References

1. S. Duttagupta, F. Ma, B. Hoex, T. Mueller and A. G. Aberle, *Energy Procedia*, 2012, **15**, 78-83.